Polarization-Resolved Plasmon-Modulated Emissions of Quantum Dots Coupled to Aluminum Dimers with Sub-20 nm Gaps

Landobasa Y. M. Tobing,[†] Dao Hua Zhang,[*,†] Kah Ee Fong,[†] Muhammad Danang Birowosuto,[‡] Yuan Gao,[†] Cuong Dang,[†,‡] and Hilmi V. Demir[†]
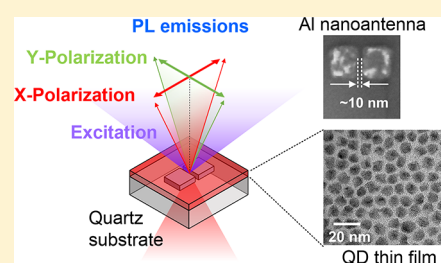
[†]School of Electrical and Electronic Engineering, Nanyang Technological University, 50 Nanyang Avenue, 639798, Singapore
[‡]CNRS International NTU Thales Research Alliance (CINTRA), Research Techno Plaza, 50 Nanyang Drive, Border X Block, 637553, Singapore

[S] Supporting Information

ABSTRACT: An aluminum dimer nanoantenna with nanogaps is an ideal platform for enhancing light−matter interaction at the nanoscale for the UV−vis spectrum, but its realization has been hindered by the surface oxidation of aluminum nanostructures, aluminum interband loss, and practical limitations in lithographic patterning. Here, we have overcome these problems and demonstrated the successful fabrication of an aluminum dimer antenna with a ~10 nm gap, which to the best of our knowledge marks the smallest features of an Al nanoantenna. We present the first in-depth study of strongly polarization-dependent emissions of colloidal quantum dots coupled with Al dimers and elucidate the individual contributions of the excitation intensity, quantum yield, and extraction efficiency enhancements from numerical and experimental perspectives. We estimate the Purcell effect corresponding to a single Al-dimer antenna as ~104 by taking into account the ensemble averaging effect and the distributions in emitter dipole orientations. This finding brings us a step closer toward a cost-effective realization of bright and ultrafast single emitters.

KEYWORDS: aluminum plasmonics, plasmonic enhancement, sub-10 nm, colloidal quantum dots, Purcell factor, photoluminescence enhancement

The high spatial overlap between highly localized plasmonic fields with nanoscale objects and the dramatic increase in the local density of states (LDOS) at plasmonic "hot spots" have led to the enhancement of light−matter interaction at the nanoscale.[1,2] The enhancements of various optical processes, such as light absorption,[3,4] photoluminescence,[5−9] higher harmonics generation,[10−14] and Raman scattering,[15−18] have been observed in plasmonic nanostructures. In particular, polarization-dependent photoluminescence enhancement of colloidal quantum dots or fluorescence molecules in the vicinity of plasmonic nanostructures has been extensively studied for its potential application in bright and ultrafast single emitters.[19−26] The integration of quantum emitters with a metal nanoantenna is carried out by embedding the quantum emitters into a polymer host and by spin-casting the quantum emitter thin film on a substrate. Dye molecules may be doped into a polymer matrix[25,27−29] or drop cast on a substrate at diluted concentrations in order to prevent emission quenching resulting from molecular aggregation,[30] while colloidal quantum dots can be applied as a thin film[31−33] or as individual emitters[34] that can be surface-functionalized onto metal surfaces.[35]

All these enhancements employed gold (Au) and silver (Ag) nanoparticles, most of which are synthesized by self-assembly processes. This is attributed to a very small damping loss in synthesized metal nanoparticles due to their crystallinity, in addition to the fact that gold and silver exhibit low damping loss in the visible and infrared range. However, the light−matter interaction with an aluminum (Al) nanoantenna has not been explored as extensively as its Au and Ag counterparts. Despite having the highest plasma oscillation frequency among plasmonic metals,[36,37] in addition to being inexpensive and corrosive-resistant, Al actually suffers from much higher damping loss compared to Au and Ag due to its interband transition at 800 nm. There are also other challenges associated with Al surface roughness and native oxidation in Al nanostructure fabrication.[38] The plasma oscillation frequency in the deep ultraviolet range makes Al plasmonics an interesting platform for studying light−matter interaction in the UV−vis spectrum, particularly when the enhancements can be facilitated from both the excitation and emission aspects. Recently, periodically arranged Al nanodisks have been investigated for enhancing the emissions of dye molecules and colloidal quantum dots,[39,40] where the enhancement was achieved through the surface lattice resonance resulting from the interference of in-plane scatterings from individual nanodisks. Stronger light−matter interaction is to be expected in an Al nanoantenna with much reduced mode volume. In this work, we present the first in-depth study of polarization-dependent CdSe/CdS colloidal quantum dot emissions coupled with an Al

dimer nanoantenna of sub-20 nm gaps. Unlike in other reported works that employed self-assembled metal nano-particles, the Al dimers in this work were defined lithographically where various dimer sizes, gaps, and orientations can be fabricated on a single chip. This enables us to study systematically the individual contributions of excitation intensity, quantum yield, and extraction efficiencies in the experimentally measured enhancements for different resonance detuning from the quantum dot emission. Specifically, we demonstrate the plasmon-modulated quantum dot emissions in the polarization-resolved PL measurements of quantum dots coupled with Al dimers, where up to ∼4.84-fold PL intensity enhancement has been achieved for an Al dimer with small detuning from the emission wavelength. Modification of emission rate with average Purcell factors of ∼1.5 is observed for PL emissions with polarizations parallel to the dimer, corresponding to an estimated Purcell factor of ∼104 by a single antenna when ensemble averaging and distributions in emitter orientations are taken into account.

■ RESULTS

The determining factors for PL enhancement in plasmonic nanoantenna are the local electric fields that signify the local density of photonic states and the radiative efficiency. Square dimer geometry is chosen for its design simplicity and strong local electric fields across the nanogaps. The schematic of a square dimer with dimer size (s) and gap (g) is shown in Figure 1a, with its long axis oriented along the x axis. Despite the known challenges in Al nanoantenna fabrication due to its surface oxidation and dimensional constraints, we have overcome this issue and demonstrated the successful fabrication of Al split ring resonator structures with features as small as ∼20 nm.[41] The transmission electron microscopy (TEM) image of the quantum dot thin film is shown in inset 1, where the size of the core−shell geometry is deduced as $d \approx 7.51 \pm 0.55$ nm from 120 quantum dots. The determining factors for the PL enhancement are large local E-field enhancement at the plasmonic hot spot and high spatial overlap between the plasmonic field and the quantum emitter. The former is achieved by decreasing the gap size, while the latter by ensuring that the gap sizes are comparable to quantum dot size. For this purpose, we fabricated Al square dimers with 10 nm gaps. The SEM micrograph of this dimer is shown in inset 2, where the sample was first spin coated with a ∼30 nm thick conductive polymer to prevent charging during scanning electron microscopy (SEM). To minimize the near-field coupling between the dimers, the periodicity (p) for these dimer structures was designed as 4× the dimer size ($p = 4s$). This design was verified by our numerical simulations, where the scattering cross section of the dimers is always smaller than the area of the unit cell ($\sigma_{scat} < p^2$). This density is also sufficient for ensuring strong signals in transmission and reflection measurements under bright field geometry. We also exploited the native surface oxidation of Al to form a ∼3 nm thick Al_2O_3 encapsulation layer for the Al nanostructure, which proves useful for reducing the emission quenching that normally occurs when quantum emitters are brought in close proximity to metals.[42,43] The electric field localization across the ∼10 nm gap also ensures a high-quality factor over mode volume (Q/V_{mod}), which translates to high LDOS.

The Al nanoantennas were fabricated on a quartz substrate, followed by spin coating of a 40 nm thick CdSe/CdS quantum dot film (∼5 monolayer thick). This film thickness was chosen
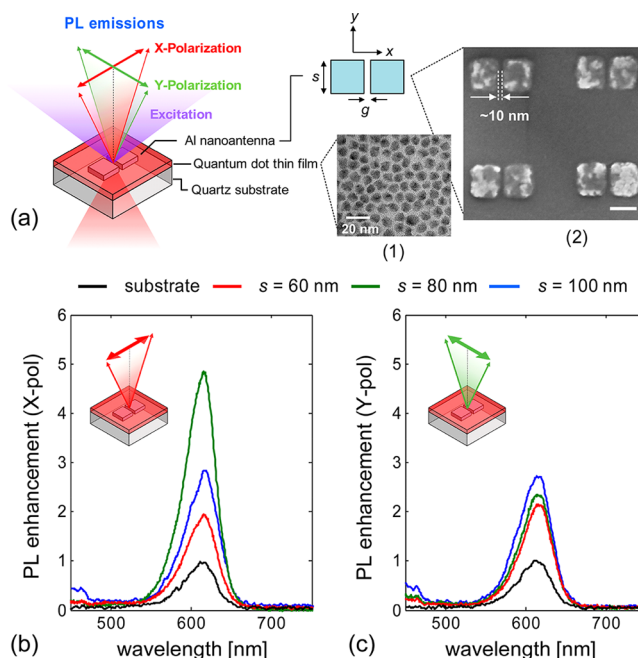

Figure 1. Polarization-resolved PL enhancements of CdSe/CdS colloidal quantum dots by aluminum square dimer structures. (a) Schematic of the Al square dimer. The square disk size is varied from s = 60 nm to s = 100 nm, while the gap spacing is varied from g = 10 nm to g = 30 nm. The thickness of the all-Al nanoantenna is t_{na} = 30 nm. Insets: (1) TEM image of the CdSe/CdS colloidal quantum dots. (2) SEM micrograph of the fabricated Al square dimers with s = 100 nm and g = 10 nm. The scale bar represents 100 nm. The black shades are the conductive polymer spin coated prior to SEM. (b, c) PL enhancements by Al square dimers for fixed gap spacing ($g \approx 10$ nm) with different size. The PL signals are normalized to the maximum PL signal from the same QD film outside the dimer regions (i.e., bare QDs on the substrate). The PL signals from the bare QD films are presented for both polarizations as reference.

to ensure a full coverage of the 30 nm thick Al nanostructures. The refractive index of the CdSe/CdS colloidal quantum dot is typically in the range of 1.7−1.95, and it is well known that coating a thin film onto a metal nanostructure introduces a red shift in its resonance wavelengths. In order to take these into account, an Al nanoantenna with smaller dimensions needs to be fabricated to compensate for such a red shift. The photoluminescence (PL) signals for quantum dots coupled with Al square dimers were characterized by a home-built PL mapping system, where a mercury lamp coupled with 434 nm bandpass filter was used as the excitation source (see Methods and Supporting Information). The quantum yield of CdSe/CdS quantum dots in this work is QY = 60%, which is sufficient for compensating the weak excitation intensity of our mercury lamp. In order to increase the PL signal contrast, the dark-field geometry is employed in the PL setup to minimize the background excitation signals.

The polarization-resolved PL enhancements from Al square dimers with $g \approx 10$ nm gaps are shown in Figure 1b and c for X- and Y-polarized PL emissions, respectively. The PL signals from the quantum dot film outside of our dimer region are also indicated by the black curves. The strong polarization dependence is indicative of the role of surface plasmons in modulating the PL emission, particularly when the enhancement for the X-polarized PL emission (PLEX) is stronger than that of the Y-polarized PL emission (PLEY). The stronger PL

enhancement for *X*-polarized emission is related to the mode characteristic of a plasmonic dimer, which can be understood in terms of dipolar coupling between the dipole modes of the constituent gold square disks. The extinction cross sections of the plasmonic dimer under *X* and *Y* polarizations are shown in Figure S2. When the dimer is excited under *X* polarization, the dipole modes interact capacitively and give rise to strong *E*-field localization in the dimer gap (Figure S2, inset 1). In addition to this field localization, the dipolar coupling also imparts a red shift to the resonance. Under *Y* polarization, however, there is no capacitive coupling since the electric dipoles are parallel to each other. This gives rise to a mode characteristic resembling that of the individual plasmonic disk (Figure S2, inset 2). Thus, the stronger field enhancement under *X* polarization is mainly caused by the capacitive coupling that gives rise to strong *E*-field localization in the dimer gap.

The effect of plasmonic resonance detuning from the quantum dot emission is exemplified in the PL enhancements for different dimer sizes, where the corresponding PLEX (PLEY) of ~2.88 (~2.72), ~4.84 (~2.32), and ~1.93 (~2.1) are observed for dimer sizes of $s = 100$ nm, $s = 80$ nm, and $s = 60$ nm, respectively. The plasmonic resonances can be further tuned toward the quantum dot emission by changing the dimer gap and exposure dose during e-beam patterning. Figure 2a and b show the transmission responses of an Al dimer ($s = 100$ nm) with different gaps, where the plasmonic resonance progressively red shifts at decreasing gap. We observed a slight blue shift as the gap decreases from $g = 30$ nm to $g = 20$ nm. Such a slight inconsistency is mainly caused by the spectral
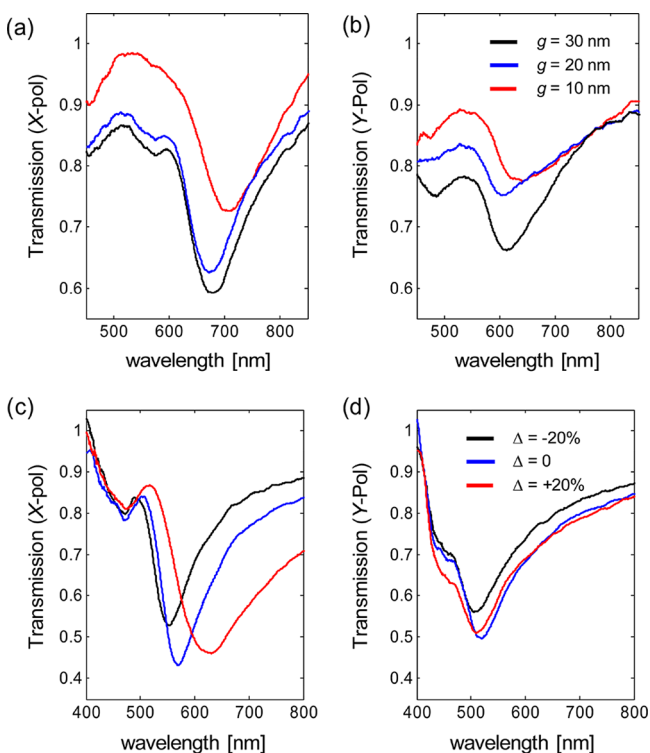
complications arising from the absorption and re-emission of light in the quantum dot film. This is confirmed in the transmission of gold dimers on an ITO substrate without quantum dot coating, showing a consistent red shift for decreasing gaps (Supporting Information). A more practical method for tuning the resonance is by changing the dimer size through exposure dose variation in the nanopatterning. Increasing e-beam dose results in larger dimer size and smaller dimer gap. The tuning range for the *X* polarization is thus expected to be larger than that for the *Y* polarization. This is because both the increase in the dimer size and the longitudinal coupling contribute to the red shift of the plasmonic resonance along the *X* polarization. This is illustrated in Figure 2c, where ~80 nm tunability was achieved by increasing the exposure dose by 40% for the resonance along the *X* polarization. In contrast, for the plasmonic resonance along the *Y* polarization, the red shift caused by the increase in dimer size is compensated by the blue shift caused by the increase of transverse dipolar coupling. This is illustrated in Figure 2d, where the resonance can be either blue- or red-shifted depending on which mechanism dominates from the increase of dimer size. We compiled the measured PL intensity enhancements from all sets of Al dimers with different gaps and sizes, which were patterned at different exposure doses, and then present their PL enhancements as a function of resonance detuning in Figure 3. The resonance tuning range for *X* and *Y*
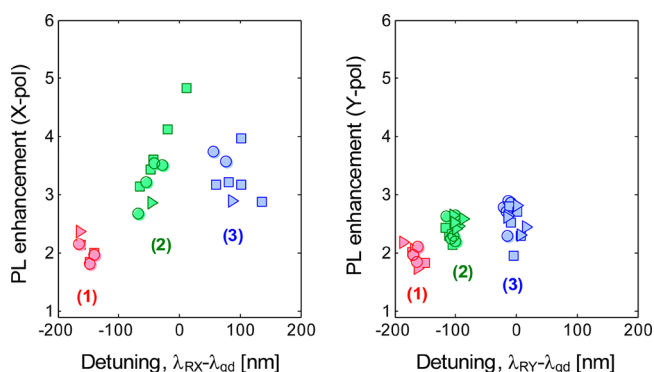
Figure 3. Polarization-resolved PL enhancement for different resonance detuning. For each combination of dimer size (*s*) and gap (*g*), ±20% exposure dose variation is introduced for the purpose of geometrical tuning. The dimers are grouped in terms of sizes (*s*) and gaps (*g*). The sizes of $s = 100$, 80, and 60 nm are indicated by (1), (2), and (3), respectively. For each size, the dimers were fabricated with three gaps, i.e., $g = 30$ nm (square), $g = 20$ nm (circle), and $g = 10$ nm (triangle).

Figure 2. Tuning plasmonic resonance toward quantum dot emission. (a, b) Role of gap spacing in resonance mode positions under *X* and *Y* polarizations in Al square dimers with $s = 100$ nm (exposed at 256 pC/cm) and gaps of 30 nm (black), 20 nm (blue), and 10 nm (red). (c, d) Role of exposure dose in tuning the resonances for Al square dimers with $s = 80$ nm and $g = 30$ nm, where the antenna were patterned at 320 pC/cm with a dose variation of ±20%.

polarizations are ~300 and ~200 nm, respectively. The dimers exposed at different e-beam dose are grouped according to their sizes, i.e., $s = 100$ nm (red), $s = 80$ nm (green), $s = 60$ nm (blue), and nominal gaps, i.e., $g = 30$ nm (squares), $g = 20$ nm (circles), $g = 10$ nm (triangles). Due to the spectral complications arising from the quantum dot absorptions and re-emissions, the resonance positions for the dimer structures were deduced from the transmission dips instead of reflection peaks. The transmission line widths of these dimers were found to be in the range of ~60−180 nm, making the *Q* factors in the range of ~4−8. As evident from Figure 3 (right panel), larger PL enhancements are observed as the resonance is tuned toward the quantum dot emissions. The same trend is observed for the *Y* polarization, although not as apparent as the *X*
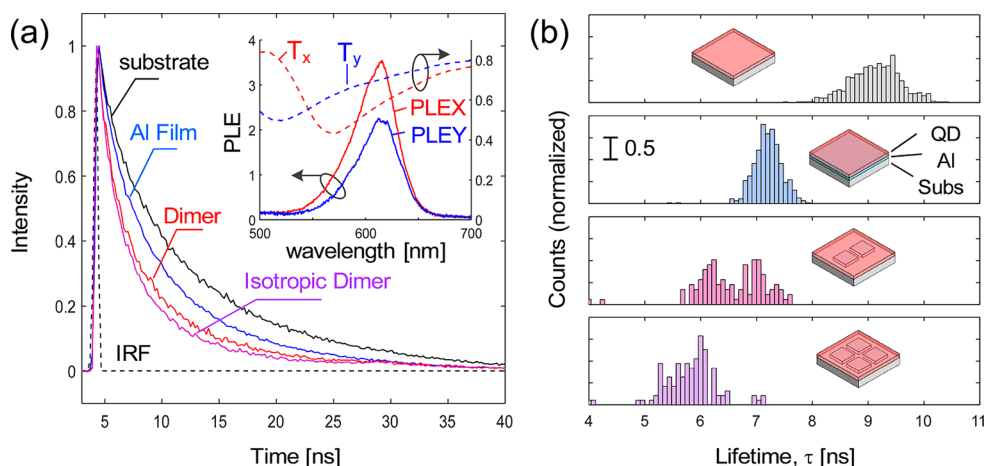
Figure 4. Fluorescence lifetime modification by Al nanostructures. (a) Time-resolved PL signals and (b) lifetime distributions of the quantum dot substrate (top panel), Al film (second panel), Al dimer (third panel), and Al isotropic dimer structures (bottom panel). Impulse response function (IRF) of the equipment is indicated by the dashed line. The average lifetime for each scenario is τ_{av} = 9.13 ns (substrate), τ_{av} = 7.2 ns (Al thin film), τ_{av} = 6.56 ns (Al dimer), τ_{av} = 5.82 ns (isotropic Al dimer). The nanoantenna for this measurement is an Al dimer with s = 80 nm and g = 20 nm, and the associated PL intensity enhancements and transmissions for X and Y polarizations are shown in the inset of (a).

polarization. This result clearly demonstrates the role of plasmonic radiation in shaping the PL emissions.

We then studied the lifetime modification from time-resolved PL signals of the quantum dots (QDs) on Al dimers with 80 nm size and 20 nm gap. The decay rates corresponding to quantum dots with and without Al nanostructures are presented in Figure 4a. Due to the unpolarized nature of the time-resolved PL measurements, we also include the decay rates of QDs on Al film and isotropic Al dimers. The isotropic dimer in this context consists of four Al square nanodisks separated by nanogaps in the X and Y directions. Based on this design, the E-field localization across the nanogaps occurs not only under X polarization as in the typical dimers but in both X and Y polarizations equally. The corresponding PL intensity enhancements for the dimer structure is presented in the inset, showing PLEX $\approx$ 3.43 and PLEY $\approx$ 2.19. The smaller intensity enhancements for this dimer (i.e., s = 80 nm, g = 20 nm) compared to those in Figure 2a,b (s = 100 nm, g = 20 nm) are attributed to the weaker E-fields across wider dimer gap and blue-shifted resonances resulting from weaker longitudinal coupling. This is illustrated by the transmission responses of the same dimer (inset of Figure 4a), showing resonance positions at ~569 and ~518 nm for X and Y polarizations, respectively.

Owing to various optical processes, the decay rate of the QDs cannot be modeled by a single-exponential model.[44] The lifetime distributions of different scenarios are presented in Figure 4b, where the area under the curve for each distribution is normalized to unity. The progressive reduction in the emission lifetime can be observed clearly as the CdSe/CdS quantum dots (τ_{av} = 9.13 ns) are coupled with the Al thin film (τ_{av} = 7.2 ns), Al dimers (τ_{av} = 6.56 ns), and Al isotropic dimers (τ_{av} = 5.82 ns). From the lifetime distribution measurements, there exist two processes responsible for the decay rate modification. The first modification originates from the metal itself, as evident from the comparison between the QD film on glass (first panel) and on the Al thin film (second panel). The second modification is caused by plasmonic resonances of the metal nanoantenna. The existence of these two processes is clearly seen in the two peaks of the lifetime distributions in the Al dimers (third panel). The peak around ~6 ns is associated with the modification based on plasmonic resonance along the

X polarization, while the peak around ~7 ns is associated with the modification based on the metal itself because the plasmonic resonance along the Y polarization is largely detuned from the quantum dot emission. Another agreement is found when the position of the second peak (~7 ns) is close to that of the distribution from the Al thin film (~7.2 ns). In order to ascertain that the second peak does originate from a far-detuned plasmonic resonance along the Y polarization, we measured the lifetime distributions of QDs on isotropic Al dimers, which exhibit the same plasmonic resonances along X and Y polarizations. As illustrated in the last panel, the lifetime distribution of the QD film on isotropic dimers exhibits only a single peak positioned around ~6 ns, in a good agreement with the position of the first peak from the Al dimer sample.

■ DISCUSSIONS

As the PL intensity depends mainly on the excitation intensity (I_{EXC}), quantum yield (QY), and the extraction efficiency (η) of the measurement setup, the measured PL enhancements are not solely caused by plasmonic resonance. Based on this understanding, the PL enhancement can be expressed as PLE = PLE(I_{EXC}) × PLE(QY) × PLE(η), where PLE(I_{EXC}) is the enhancement of excitation intensity, PLE(QY) is the enhancement of quantum yield, and PLE(η) is the enhancement of extraction efficiency. The PL enhancements are dominated by the excitation intensity enhancement when the plasmonic resonance is much shorter than the emission wavelength and close to the excitation wavelength. This is clearly seen in the ~2-fold PL enhancement of QD coupled to 60 nm sized dimers (Figure 3). As the plasmonic resonances are tuned toward emission wavelength, the PL enhancements are mainly determined by PLE(QY) × PLE(η), where the highly localized electric field results in the enhancement of both quantum yield due to the increased local density of states and antenna radiation due to the strong electric dipole. The role of the local field enhancement in the PLE can be further studied by comparing the PLEX and PLEY of different dimers whose resonances are of the same detuning. In Figure 5, we present the PLEX = 4.84, corresponding to dimers with s = 80 nm and g = 10 nm (Figure 1b, s = 80 nm), and the PLEY = 2.71, corresponding to dimers with s = 100 nm and g = 10 nm
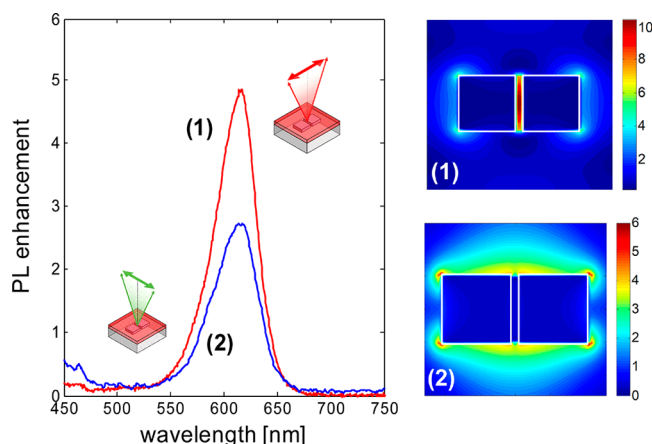
Figure 5. Role of local electric field enhancement in PL enhancements. Two Al dimers were chosen such that the X-polarized and Y-polarized emissions occur at near-zero detuning from the QD emission: (1) $s = 80$ nm, $g = 10$ nm, X-polarization; (2) $s = 100$ nm, $g = 10$ nm, Y-polarization. The inset shows the $|E|$-field distributions for both resonances.

(Figure 1c, $s = 100$ nm), both of which have near-zero detuning with the quantum dot emission wavelength. The calculated electric field distributions from the insets reveal that the local electric field is ~2× stronger for the X polarization than for Y polarization. From the perspective of the local density of states $(\propto |E|^2)$,[45] the spatially averaged enhancement per unit area $\left(\propto (1/p^2) \int_{\text{cell}} |E|^2 \, dx \, dy \right)$ for X polarization is expected to be ~1.44× higher than that for the Y polarization.

In addition to increasing LDOS, strong local E-fields also reshape the QD emission pattern in the vicinity of the Al nanoantenna. The extraction efficiency for each dimer can be estimated from the far-field projection (see Methods). Using NA = 0.55 for the 50× objective lens, the extraction efficiencies for each dimer can be calculated as $\eta_{\text{dimer}}^X \approx 33.7\%$ (for X-polarized emissions of a dimer with $s = 80$ nm and $g = 10$ nm) and $\eta_{\text{dimer}}^Y \approx 24.2\%$ (for Y-polarized emissions of a dimer with $s = 100$ nm and $g = 10$ nm), making the extraction efficiency ~1.39× higher for the X polarization. Combining the increase in LDOS (~1.44×) and extraction efficiency (~1.39×) makes the overall PL intensity ~2× stronger for the X polarization compared to the Y polarization. This is in reasonable agreement with the ~1.78× stronger PL intensities shown in Figure 5. The extraction efficiency of a QD film without an Al nanoantenna with the same objective lens is estimated as $\eta_{\text{QD}} \approx 11.5\%$, making the extraction efficiency enhancements of PLEX$(\eta) = \eta_{\text{dimer}}^X / \eta_{\text{QD}} \approx 2.94$ (for X-polarized emission) and PLEY$(\eta) = \eta_{\text{dimer}}^Y / \eta_{\text{QD}} \approx 2.1$ (for Y-polarized emission). By assuming PLE$(I_{\text{EXC}}) \approx 1$ for near-zero detuning, the quantum yield enhancements for the 10 nm gap dimers can be estimated as PLEX$(\text{QY}) = \text{PLEX}/\text{PLEX}(\eta) \approx 1.65$ and PLEY$(\text{QY}) = \text{PLEY}/\text{PLEX}(\eta) \approx 1.29$.

Similarly, the extraction efficiencies for the 20 nm gap dimers (in Figure 4) are $\eta_{\text{dimer}}^X \approx 34.9\%$ and $\eta_{\text{dimer}}^Y \approx 12.1\%$, giving extraction efficiency enhancements of PLEX$(\eta) = 3.04$ and PLEY$(\eta) = 1.06$. The smaller enhancements in the 20 nm gap dimers are expected, as their resonances are more detuned from the emission wavelength, particularly for the Y polarization, where the extraction efficiency is not much different than that of the uncoupled QDs. For the X-polarized emission, owing to the large detuning from the excitation wavelength ($\Delta\lambda_{\text{EXC}} \approx$

135 nm) and small detuning from the emission wavelength ($\Delta\lambda_{\text{QD}} \approx 49$ nm), we can still assume PLEX$(I_{\text{EXC}}) \approx 1$ and estimate the quantum yield enhancement as PLEX$(\text{QY}) = \text{PLEX}/\text{PLEX}(\eta) \approx 1.13$. This is consistent with the much larger quantum yield enhancement for the 10 nm gap dimer, which results from stronger local E-fields across the gap and smaller mode volume. For the Y-polarized emission, the contribution from the excitation enhancement cannot be ignored, as the detuning from the emission ($\Delta\lambda_{\text{QD}} \approx 100$ nm) is larger than that from the excitation ($\Delta\lambda_{\text{EXC}} \approx 84$nm). Thus, the contributions from the excitation and quantum yield enhancements for the Y-polarization are estimated as PLEY$/\text{PLEY}(\eta) = \text{PLEY}(I_{\text{EXC}}) \times \text{PLEY}(\text{QY}) = 2.07$.

It is also possible to decouple PLE (QY) and PLE (η) based on the relation between PLE (QY) and the decay rate modification. From the perspective of decay rate, quantum yield is defined as $\text{QY} = k_{\text{rad}}/(k_{\text{rad}} + k_{\text{nrad}})$, where k_{rad} and k_{nrad} are the radiative and nonradiative recombination rates of the quantum dots, respectively. In the vicinity of the metal nanoantenna, the emission rate of the quantum dots is enhanced by a Purcell factor defined by $F_{\text{p}} = (k_{\text{na}} + k_{\text{rad}})/k_{\text{rad}}$, where k_{na} is the radiative decay rate caused by the nanoantenna. The modified quantum yield in the presence of the metal nanoantenna is expressed as $\text{QY}' = (k_{\text{na}} + k_{\text{rad}})/(k_{\text{na}} + k_{\text{rad}} + k_{\text{nrad}})$, and the quantum yield enhancement is PLE$(\text{QY}) = \text{QY}'/\text{QY}$. The Purcell factor is thus related to the quantum yield by $F_{\text{p}} = (1 - \text{QY})/(1 - \text{QY}')$,[46] indicating that both the emission rate modification and PL intensities occur simultaneously. However, a large Purcell factor does not necessarily mean large PL intensity enhancements, as the maximum PL intensity enhancement depends on the initial quantum yield of the emitter. Based on the CdSe/CdS quantum dot used in this work (QY ≈ 0.6), the maximum quantum yield enhancement (corresponding $F_{\text{p}} = \infty$) is thus limited to PLE$(\text{QY})_{\text{MAX}} \approx 1.67$.

From the PL traces in Figure 4, the average Purcell factor of the 20 nm gap dimers can be directly measured as $F_{\text{P},X} \approx 1.5$ (for X-polarized emission) and $F_{\text{P},Y} \approx 1.28$ (for the Y-polarized emission). To ensure the reproducibility of these Purcell factors, the same sample was characterized by another time-resolved micro-PL setup based on a free-space excitation technique, where comparable Purcell factors of $F_{\text{P},X} \approx 1.4$ and $F_{\text{P},Y} \approx 1.29$ were measured (Figure S4, Supporting Information). Referring to the Purcell factor for the X-polarized emission (Figure 4), $F_{\text{P},X} \approx 1.5$ corresponds to a modified average quantum yield of $\text{QY}' = 0.73$ and a quantum yield enhancement of PLEX$(\text{QY}) \approx 1.2$. This is again in agreement with PLEX$(\text{QY}) \approx 1.13$ that was estimated previously. The extraction efficiency enhancement for X-polarized emission is deduced as PLEX$(\eta) = \text{PLEX}/\text{PLEX}(\text{QY}) \approx 2.85$. For the Y-polarized emission, $F_{\text{P},Y} \approx 1.28$ corresponds to a modified quantum yield of $\text{QY}' \approx 0.69$ and a quantum yield enhancement of PLEY$(\text{QY}) \approx 1.15$. As the plasmonic resonance is close to the excitation wavelength ($\Delta\lambda_{\text{EXC}} \approx 84$nm), we expect the PL enhancement for Y-polarized emission to be contributed mostly by the excitation intensity enhancement. This is supported by the fact that the detuning ($\Delta\lambda_{\text{QD}} \approx 100$ nm) is larger than the line width of the PL response ($\Delta\lambda_{\text{PL}} = 60$ nm). Using PLEY$(\eta) = 1.06$ from the previous calculation, we can deduce the excitation intensity enhancement of PLEY$(I_X) \approx 1.8$ for a 20 nm gap dimer. This is in agreement with the ~2-fold intensity enhancements for 60

nm sized dimers that have small detuning from the excitation source ($\Delta\lambda_{EXC} < 40$ nm).

The ideal Purcell factor is calculated based on the assumptions that the emitter is located at the spatial maximum with its dipole orientation perfectly aligned with the nanoantenna local E-fields. Based on the calculated $V_{mod}^X = 2.1 \times 10^{-3}(\lambda/n)^3$ and measured $Q_{meas}^X \approx 6.05$, the ideal Purcell factors for a single dimer antenna with a 20 nm gap is $F_{P,X} \approx 104.9$ for X-polarized emission. This is ~70× higher than the measured Purcell factor in Figure 4 ($F_{P,X} \approx 1.5$). This is indicative of the ensemble averaging effect, where only quantum dots located within the plasmonic hot spots are significantly modified. By assuming quantum dots to be uniformly distributed within the thin film, the fraction of quantum dots in the plasmonic hot spot can be estimated as $f = V_{mod}/(t_{na}p^2) \approx 0.031$, giving the spatially averaged Purcell factor of $F_{P,AV} = fF_P + (1 - f) \approx 4.18$. Another equally important factor is the distribution of emitter dipole orientations in the QD thin film. While the dipole orientations are likely to be random in all directions (isotropic) for quantum dots suspended in a solution or when the quantum dot film is very thick, the same property may not hold for quantum dot films with a few monolayers' thickness. By assuming $\cos^2 \theta$ dependence in the emission rate for a dipole at angle θ from the local E-field,[23] the average dipole orientation for a five-monolayer thick quantum dot film can be estimated as $\theta \approx 53°$ from the XY plane. Better alignment between the emitter and the nanoantenna is to be expected when the QD film thickness is reduced to only a monolayer thick. This may be achieved through surface functionalization for ensuring good adhesion between quantum dots and the substrate.

CONCLUSION

Photoluminescence emissions of CdSe/CdS colloidal quantum dots coupled with an Al plasmonic dimer nanoantenna of sub-20 nm gaps have been experimentally demonstrated together with numerical simulation. The role of plasmonic radiation in shaping the PL responses is evidenced by the strong polarization dependences in the PL emissions. The enhancements of the excitation intensity, the quantum yield, and the extraction efficiency have been investigated in Al dimers with different plasmonic resonances over ~300 nm of wavelength detuning, and PL intensity enhancements up to ~4.84× and ~2.72× have been measured for emissions along the X and Y polarizations. By tuning the size of Al dimers, we can increase the PL by enhancing either the excitation intensity or emission extraction efficiency. We have shown that the ~2× PL enhancements for the 60 nm sized dimers are dominated by the excitation intensity enhancement. Based on this understanding, it is possible to design an Al nanoantenna with resonance modes matching the excitation and emission wavelengths. In addition to further improvement in the PL emission efficiency, plasmonic nanostructures with multi-resonance modes could be useful for enhancing other process, such as frequency upconversion[47,48] and photodetection.[49] By comparing the X-polarized and Y-polarized PL emissions of two different dimers with the same near-zero detuning, the role of the local E-field in increasing LDOS and reshaping the QD emission pattern has been discussed. The faster decay rates and PL intensity enhancements of quantum dots coupled with an Al dimer nanoantenna indicate that the rate modification is indeed caused by antenna radiation instead of by nonradiative quenching. Spatially averaged Purcell factors of ~1.5 and ~1.28 have been measured for X-polarized and Y-polarized

emissions from Al dimers with a 20 nm gap. By relating the Purcell factor with the quantum yield, we have deduced the enhancement in the quantum yield that results from the higher LDOS, where quantum yields increase from 60% in the QD films to ~73% and ~69% for X-polarized and Y-polarized emissions of QDs on dimers, respectively. Finally, nonidealities associated with spatial averaging and dipole orientation distributions have been identified for causing a ~70× smaller Purcell factor in the experimental measurements.

METHODS

Nanofabrication of an Al Nanoantenna with CdSe/CdS Quantum Dots. The Al nanostructures were fabricated on a quartz glass substrate by sonicated cold development processes,[41] where the patterning was done by an electron beam lithography system (Raith e_LiNE) with 20 keV beam energy and 30pA beam current. The patterned samples were evaporated by 30 nm thick aluminum at a 0.05 nm/s rate, followed by lift-off in n-methylpyrrolidone for 10 min. Different types of Al nanoantennas were fabricated on the same chip, where each nanostructure occupies a 100×100 μm^2 footprint. A CdSe/CdS quantum dot film (30 mg/mL concentration) was then spin coated at 2000 rpm speed, giving a 40 nm film thickness, as verified by a surface profilometer.

Photoluminescence and Optical Characterization. Both the photoluminescence and transmission measurements were carried out by the same microscope system. In the transmission measurements, the halogen lamp was focused by a condenser into the sample and the transmission signals were collected by 10× objective lens (NA 0.3) under bright-field geometry. The signals were directed to the transmission grating and CCD sensor, and the piezostage was scanned in order to get the transmission image. The transmission for a particular nanoantenna array was obtained from the pixels corresponding to the structure, followed by normalization with respect to the signals from the substrate (on which the quantum dot film was spin coated). The image based on the 10× objective lens consists of 1024 lines, where the scanning time for each line is 0.05 s. All the signals are averaged within a 20 by 20 pixel area. In the photoluminescence measurement, we used a mercury lamp coupled (with 434 nm bandpass filter) focused by a 50× objective lens (NA 0.55). Although PL measurements can be done in both dark- or bright-field geometries, the measurements based on dark-field setting exhibit a higher signal-to-noise ratio due to the much smaller background excitation. As the excitation source (434 nm) is sufficiently far from quantum dot emission (618 nm), a long pass filter (LPF) is not required. The PL measurements in our experiment were done with and without an LPF (with onset wavelength at 500 nm), showing good consistency in the PL enhancements. The PL intensity enhancement is obtained by normalizing the pixels corresponding to the Al nanoantenna with the pixels corresponding to the quantum dot substrate. The image based on the 50× objective lens consists of 720 lines, where the scanning time for each line is 0.5 s (with gain ON). As in transmission measurements, the signals are averaged within a 20×20 pixel area.

Time-Resolved Photoluminescence. The time-resolved PL measurements were obtained by confocal scanning fluorescence lifetime imaging microscopy. The sample was excited by a pulsed laser with a wavelength of 375 nm, repetition rate of 20 MHz, and pulse duration of 100 ps. The instrument response was 200 ps. The lifetime mapping area was 900×900 μm^2. The lifetime of each pixel within the mapping

area was recorded, and their distribution was obtained from an area that corresponds to a certain nanostructure.

Numerical Simulations. We performed finite difference time domain simulations (FDTD Solutions, Lumerical Inc.) to calculate the optical responses of an aluminum square dimer antenna. The scattering properties were calculated using the total-field-scattered-field module, where the inward and outward power flows were calculated to deduce absorption (σ_{abs}) and scattering (σ_{scat}) cross sections. The extinction cross section (σ_{ext}) is $\sigma_{ext} = \sigma_{abs} + \sigma_{scat}$. The radiation efficiency of the Al nanoantenna was calculated as $\eta_{rad} = \sigma_{scat}/\sigma_{ext}$. The periodic boundary condition was enforced in the simulation in order to take into account the effect of periodicity. The permittivity of aluminum and quartz glass was based on the Palik model. The quantum dot film is assumed as a dielectric layer with a refractive index of $n_{qd} \approx 1.75$, which was obtained from fitting the red-shifted resonances of the Al nanoantenna after the quantum dot film is spin coated. The extraction efficiencies were calculated as the fraction of the radiation collected by the objective lens. The radiated power was calculated by integrating the forward and backward far-field projections over all the direction cosines, i.e., $-1 \leq u_{x,y,z} \leq 1$, while the collected power was calculated by integrating the far-field projection over a circular area that represents the numerical aperture of the lens, i.e., $u_x^2 + u_y^2 < NA^2$. The direction cosines are defined as $u_x = \sin\theta\cos\phi$, $u_y = \sin\theta\sin\phi$, and $u_z = \sqrt{1 - u_x^2 - u_y^2}$. The extraction efficiency for the quantum dot under specific polarization was calculated by representing the quantum dot as a dipole source with the same polarization, followed by the same routine as for the Al dimers. The Purcell factor for the slightly detuned case was calculated as

$$F_P(\omega) = (3/8\pi)(\lambda/n)^3(\omega/V_{mod})\rho_{cav}(\omega)$$

where

$$V_{mod} = t_{na} \int_{cell} \epsilon |E|^2 \mathrm{d}x \, \mathrm{d}y / \max(\epsilon |E|^2)$$

is the mode volume, and $\rho_{cav}(\omega) = (2/\pi)\Delta\omega_{cav}[4(\omega - \omega_{cav})^2 + \Delta\omega_{cav}^2]^{-1}$ is the total density of states of the resonance mode.[9] The case of $\omega = \omega_{cav}$ leads to the ideal Purcell factor $F_P = (3/4\pi^2)(\lambda/n)^3(Q/V_{mod})$.

ASSOCIATED CONTENT

Ⓢ Supporting Information

The Supporting Information is available free of charge on the ACS Publications website at DOI: 10.1021/acsphotonics.8b00009.

Additional information (PDF)

AUTHOR INFORMATION

Corresponding Author

*E-mail: edhzhang@ntu.edu.sg.

ORCID

Landobasa Y. M. Tobing: 0000-0002-3113-1252
Muhammad Danang Birowosuto: 0000-0002-9997-6841
Yuan Gao: 0000-0001-9407-1528
Cuong Dang: 0000-0001-6183-4082
Hilmi V. Demir: 0000-0003-1793-112X

Author Contributions

D.H.Z. initiated and supervised the project. L.Y.M.T. conceived the idea and fabricated and characterized the transmission and photoluminescence mapping properties of the plasmonic nanostructures. K.E.F. synthesized the CdSe/CdS quantum dots, while L.Y.M.T. built the photoluminescence mapping setup. M.D.B., Y.G., C.D., and H.V.D. facilitated and characterized time-resolved photoluminescence, while M.D.B. and C.D. contributed technical discussions on photoluminescence and Purcell factor. L.Y.M.T. wrote the manuscript, with input from all the authors. All the authors read and approved the manuscript.

Notes

The authors declare no competing financial interest.

REFERENCES

(1) Sun, G.; Khurgin, J. B. Origin of Giant Difference between Fluorescence, Resonance, and Nonresonance Raman Scattering Enhancement by Surface Plasmons. *Phys. Rev. A: At., Mol., Opt. Phys.* **2012**, *85* (6), 63410.

(2) Koenderink, A. F. Single-Photon Nanoantennas. *ACS Photonics* **2017**, *4*, 710−722.

(3) Chang, C.-C.; Sharma, Y. D.; Kim, Y.-S.; Bur, J. A.; Shenoi, R. V.; Krishna, S.; Huang, D.; Lin, S.-Y. A Surface Plasmon Enhanced Infrared Photodetector Based on InAs Quantum Dots. *Nano Lett.* **2010**, *10* (5), 1704−1709.

(4) Ren, F. F.; Ang, K. W.; Ye, J.; Yu, M.; Lo, G. Q.; Kwong, D. L. Split Bull's Eye Shaped Aluminum Antenna for Plasmon-Enhanced Nanometer Scale Germanium Photodetector. *Nano Lett.* **2011**, *11* (3), 1289−1293.

(5) Huang, J.; Tung, K. H. P.; Deng, L.; Xiang, N.; Dong, J.; Danner, A. J.; Teng, J. Surface Plasmon Enhanced Photoluminescence in Gold Capped InGaAs Quantum Well Nanodisk Array. *Opt. Mater. Express* **2013**, *3* (12), 2003.

(6) Li, G.-C.; Zhang, Y.-L.; Jiang, J.; Luo, Y.; Lei, D. Y. Metal-Substrate-Mediated Plasmon Hybridization in a Nanoparticle Dimer for Photoluminescence Line-Width Shrinking and Intensity Enhancement. *ACS Nano* **2017**, *11* (3), 3067−3080.

(7) Huang, D.; Byers, C. P.; Wang, L. Y.; Hoggard, A.; Hoener, B.; Dominguez-Medina, S.; Chen, S.; Chang, W. S.; Landes, C. F.; Link, S. Photoluminescence of a Plasmonic Molecule. *ACS Nano* **2015**, *9* (7), 7072−7079.

(8) Hu, H.; Duan, H.; Yang, J. K. W.; Shen, Z. X. Plasmon-Modulated Photoluminescence of Individual Gold Nanostructures. *ACS Nano* **2012**, *6* (11), 10147−10155.

(9) Decker, M.; Staude, I.; Shishkin, I. I.; Samusev, K. B.; Parkinson, P.; Sreenivasan, V. K. A.; Minovich, A.; Miroshnichenko, A. E.; Zvyagin, A.; Jagadish, C.; Neshev, D. N.; Kivshar, Y. S. Dual-Channel Spontaneous Emission of Quantum Dots in Magnetic Metamaterials. *Nat. Commun.* **2013**, *4.*10.1038/ncomms3949

(10) Valev, V. K.; Clercq, B. D.; Zheng, X.; Denkova, D.; Osley, E. J.; Vandendriessche, S.; Silhanek, a V.; Volskiy, V.; Warburton, P. a.; Vandenbosch, G. a E.; Ameloot, M.; Moshchalkov, V. V.; Verbiest, T. The Role of Chiral Local Field Enhancements below the Resolution Limit of Second Harmonic Generation Microscopy. *Opt. Express* **2012**, *20* (1), 256−264.

(11) Metzger, B.; Schumacher, T.; Hentschel, M.; Lippitz, M.; Giessen, H. Third Harmonic Mechanism in Complex Plasmonic Fano Structures. *ACS Photonics* **2014**, *1* (6), 471−476.

(12) Slablab, A.; Le Xuan, L.; Zielinski, M.; de Wilde, Y.; Jacques, V.; Chauvat, D.; Roch, J.-F. Second-Harmonic Generation from Coupled Plasmon Modes in a Single Dimer of Gold Nanospheres. Opt. *Opt. Express* **2012**, *20* (1), 220.

(13) Butet, J.; Brevet, P.-F.; Martin, O. J. F. Optical Second Harmonic Generation in Plasmonic Nanostructures: From Fundamental Principles to Advanced Applications. *ACS Nano* **2015**, *9* (11), 10545–10562.

(14) Sartorello, G.; Olivier, N.; Zhang, J.; Yue, W.; Gosztola, D. J.; Wiederrecht, G. P.; Wurtz, G.; Zayats, A. V. Ultrafast Optical Modulation of Second- and Third-Harmonic Generation from Cut-Disk-Based Metasurfaces. *ACS Photonics* **2016**, *3* (8), 1517–1522.

(15) Doherty, M. D.; Murphy, A.; Pollard, R. J.; Dawson, P. Surface-Enhanced Raman Scattering from Metallic Nanostructures: Bridging the Gap between the near-Field and Far-Field Responses. *Phys. Rev. X* **2013**, *3* (1), 1–12.

(16) Yue, W.; Yang, Y.; Wang, Z.; Chen, L.; Wang, X. Gold Split-Ring Resonators (SRRs) as Substrates for Surface-Enhanced Raman Scattering. *J. Phys. Chem. C* **2013**, *117* (42), 21908–21915.

(17) Wen, X.; Li, G.; Zhang, J.; Zhang, Q.; Peng, B.; Wong, L. M.; Wang, S.; Xiong, Q. Transparent Free-Standing Metamaterials and Their Applications in Surface-Enhanced Raman Scattering. *Nanoscale* **2014**, *6* (1), 132–139.

(18) Clark, A. W.; Glidle, A.; Cumming, D. R. S.; Cooper, J. M. Plasmonic Split-Ring Resonators as Dichroic Nanophotonic DNA Biosensors. *J. Am. Chem. Soc.* **2009**, *131* (48), 17615–17619.

(19) Muskens, O. L.; Giannini, V.; Sánchez-Gil, J. A.; Gómez Rivas, J.; Sa, J. A. Strong Enhancement of the Radiative Decay Rate of Emitters by Single Plasmonic Nanoantennas. *Nano Lett.* **2007**, *7* (9), 2871–2875.

(20) Hoang, T. B.; Akselrod, G. M.; Mikkelsen, M. H. Ultrafast Room-Temperature Single Photon Emission from Quantum Dots Coupled to Plasmonic Nanocavities. *Nano Lett.* **2016**, *16* (1), 270–275.

(21) Belacel, C.; Habert, B.; Bigourdan, F.; Marquier, F.; Hugonin, J.-P.; Michaelis de Vasconcellos, S.; Lafosse, X.; Coolen, L.; Schwob, C.; Javaux, C.; Dubertret, B.; Greffet, J.-J.; Senellart, P.; Maitre, A. Controlling Spontaneous Emission with Plasmonic Optical Patch Antennas. *Nano Lett.* **2013**, *13* (4), 1516–1521.

(22) Rose, A.; Hoang, T. B.; McGuire, F.; Mock, J. J.; Ciracì, C.; Smith, D. R.; Mikkelsen, M. H. Control of Radiative Processes Using Tunable Plasmonic Nanopatch Antennas. *Nano Lett.* **2014**, *14* (8), 4797–4802.

(23) Akselrod, G. M.; Argyropoulos, C.; Hoang, T. B.; Ciracì, C.; Fang, C.; Huang, J.; Smith, D. R.; Mikkelsen, M. H. Probing the Mechanisms of Large Purcell Enhancement in Plasmonic Nanoantennas. Nat. *Nat. Photonics* **2014**, *8* (11), 835–840.

(24) Kinkhabwala, A.; Yu, Z.; Fan, S.; Avlasevich, Y.; Müllen, K.; Moerner, W. E. Large Single-Molecule Fluorescence Enhancements Produced by a Bowtie Nanoantenna. Nat. *Nat. Photonics* **2009**, *3* (11), 654–657.

(25) Zhou, X.; Deeb, C.; Kostcheev, S.; Wiederrecht, G. P.; Adam, P.-M.; Beál, J.; Me Plain, J.; Gosztola, D. J.; Grand, J.; Feíidj, N.; Wang, H.; Vial, A.; Bachelot, R.; Béal, J.; Plain, J.; Gosztola, D. J.; Grand, J.; Félidj, N.; Wang, H.; Vial, A.; Bachelot, R. Selective Functionalization of the Nanogap of a Plasmonic Dimer. *ACS Photonics* **2015**, *2* (1), 121–129.

(26) Suh, J. Y.; Kim, C. H.; Zhou, W.; Huntington, M. D.; Co, D. T.; Wasielewski, M. R.; Odom, T. W. Plasmonic Bowtie Nanolaser Arrays. *Nano Lett.* **2012**, *12* (11), 5769–5774.

(27) Yuan, C. T.; Wang, Y. C.; Cheng, H. W.; Wang, H. S.; Kuo, M. Y.; Shih, M. H.; Tang, J. Modification of Fluorescence Properties in Single Colloidal Quantum Dots by Coupling to Plasmonic Gap Modes. *J. Phys. Chem. C* **2013**, *117* (24), 12762–12768.

(28) Wang, X.; Shih, C. K.; Xu, J.; Xiao, M. Enhanced Dipole-Dipole Interaction of CdSe/CdS Nanocrystal Quantum Dots inside a Planar Microcavity. *Appl. Phys. Lett.* **2006**, *89* (11), 2006–2008.

(29) Shundo, A.; Okada, Y.; Ito, F.; Tanaka, K. Fluorescence Behavior of Dyes in Thin Films of Various Polymers. *Macromolecules* **2012**, *45* (1), 329–335.

(30) Chapman, M.; Mullen, M.; Novoa-Ortega, E.; Alhasani, M.; Elman, J. F.; Euler, W. B. Structural Evolution of Ultrathin Films of Rhodamine 6G on Glass. *J. Phys. Chem. C* **2016**, *120* (15), 8289–8297.

(31) Kwangdong Roh, C. D.; Joonhee Lee, S. C.; Jonathan, S.; Steckel; Seth Coe-Sullivan, A. N. Surface-Emitting Red, Green, and Blue Colloidal Quantum Dot Distributed Feedback Lasers. *Opt. Express* **2014**, *22* (15), 18800.

(32) Gao, Y.; Tobing, L. Y. M.; Kiffer, A. A.; Zhang, D. H.; Dang, C.; Demir, H. V.; M Tobing, L. Y.; Kiffer, A. A.; Hua Zhang, D.; Dang, C.; Volkan Demir, H. Azimuthally Polarized, Circular Colloidal Quantum Dot Laser Beam Enabled by a Concentric Grating. *ACS Photonics* **2016**, *3* (12), 2255–2261.

(33) Birowosuto, M. D.; Takiguchi, M.; Olivier, A.; Tobing, L. Y.; Kuramochi, E.; Yokoo, A.; Hong, W.; Notomi, M. Temperature-Dependent Spontaneous Emission of PbS Quantum Dots inside Photonic Nanostructures at Telecommunication Wavelength. *Opt. Commun.* **2017**, *383*, 555–560.

(34) Hoang, T. B.; Akselrod, G. M.; Argyropoulos, C.; Huang, J.; Smith, D. R.; Mikkelsen, M. H. Ultrafast Spontaneous Emission Source Using Plasmonic Nanoantennas. *Nat. Commun.* **2015**, *6*, 7788.

(35) Ureña, E. B.; Kreuzer, M. P.; Itzhakov, S.; Rigneault, H.; Quidant, R.; Oron, D.; Wenger, J. Excitation Enhancement of a Quantum Dot Coupled to a Plasmonic Antenna. *Adv. Mater.* **2012**, *24* (44), 314–320.

(36) Zorić, I.; Zäch, M.; Kasemo, B.; Langhammer, C. Gold, Platinum, and Aluminum Nanodisk Plasmons: Material Independence, Subradiance, and Damping Mechanisms. *ACS Nano* **2011**, *5* (4), 2535–2546.

(37) Knight, M. W.; King, N. S.; Liu, L.; Everitt, H. O.; Nordlander, P.; Halas, N. J. Aluminum for Plasmonics. *ACS Nano* **2014**, *8* (1), 834–840.

(38) Knight, M. W.; Liu, L.; Wang, Y.; Brown, L.; Mukherjee, S.; King, N. S.; Everitt, H. O.; Nordlander, P.; Halas, N. J. Aluminum Plasmonic Nanoantennas. *Nano Lett.* **2012**, *12* (11), 6000–6004.

(39) Lozano, G.; Louwers, D. J.; Rodríguez, S. R.; Murai, S.; Jansen, O. T.; Verschuuren, M. A.; Gómez Rivas, J. Plasmonics for Solid-State Lighting: Enhanced Excitation and Directional Emission of Highly Efficient Light Sources. *Light: Sci. Appl.* **2013**, *2* (5), e66.

(40) Abass, A.; Rodriguez, S. R. K.; Ako, T.; Aubert, T.; Verschuuren, M.; Van Thourhout, D.; Beeckman, J.; Hens, Z.; Gómez Rivas, J.; Maes, B. Active Liquid Crystal Tuning of Metallic Nanoantenna Enhanced Light Emission from Colloidal Quantum Dots. *Nano Lett.* **2014**, *14* (10), 5555–5560.

(41) Tobing, L. Y. M.; Zhang, D.-H. Preferential Excitation of the Hybrid Magnetic-Electric Mode as a Limiting Mechanism for Achievable Fundamental Magnetic Resonance in Planar Aluminum Nanostructures. *Adv. Mater.* **2016**, *28* (5), 889–896.

(42) Dulkeith, E.; Morteani, A. C.; Niedereichholz, T.; Klar, T. A.; Feldmann, J.; Levi, S. A.; van Veggel, F. C. J. M.; Reinhoudt, D. N.; Möller, M.; Gittins, D. I. Fluorescence Quenching of Dye Molecules near Gold Nanoparticles: Radiative and Nonradiative Effects. *Phys. Rev. Lett.* **2002**, *89* (20), 203002.

(43) Aldeek, F.; Ji, X.; Mattoussi, H. Quenching of Quantum Dot Emission by Fluorescent Gold Clusters: What It Does and Does Not Share with the Förster Formalism. *J. Phys. Chem. C* **2013**, *117* (29), 15429–15437.

(44) van Driel, A. F.; Nikolaev, I. S.; Vergeer, P.; Lodahl, P.; Vanmaekelbergh, D.; Vos, W. L. Statistical Analysis of Time-Resolved Emission from Ensembles of Semiconductor Quantum Dots: Interpretation of Exponential Decay Models. *Phys. Rev. B: Condens. Matter Mater. Phys.* **2007**, *75* (3), 35329.

(45) Koenderink, A. F. On the Use of Purcell Factors for Plasmon Antennas. *Opt. Lett.* **2010**, *35* (24), 4208–4210.

(46) Okamoto, K.; Vyawahare, S.; Scherer, A. Surface-Plasmon Enhanced Bright Emission from CdSe Quantum-Dot Nanocrystals. *J. Opt. Soc. Am. B* **2006**, *23* (8), 1674.

(47) Kang, F.; He, J.; Sun, T.; Bao, Z. Y.; Wang, F.; Lei, D. Y. Plasmonic Dual-Enhancement and Precise Color Tuning of Gold Nanorod@SiO2Coupled Core−Shell−Shell Upconversion Nanocrystals. *Adv. Funct. Mater.* **2017**, *27* (36), 1−11.

(48) He, J.; Zheng, W.; Ligmajer, F.; Chan, C.-F.; Bao, Z.; Wong, K.-L.; Chen, X.; Hao, J.; Dai, J.; Yu, S.-F.; Lei, D. Y. Plasmonic Enhancement and Polarization Dependence of Nonlinear Upconversion Emissions from Single Gold nanorod@SiO2@CaF2:Yb3+,Er3+ Hybrid Core−shell−satellite Nanostructures. *Light: Sci. Appl.* **2016**, *6* (5), e16217.

(49) Tong, J.; Tobing, L. Y. M.; Luo, Y.; Zhang, D.; Zhang, D. H. Single Plasmonic Structure Enhanced Dual-Band Room Temperature Infrared Photodetection. *Sci. Rep.* **2018**, *8* (1), 1548.